

# The mantle transition zone beneath eastern North America: Receiver functions and tomographic velocity models

Alexander L. Burky<sup>a,\*</sup>, Jessica C. E. Irving<sup>b</sup>, Frederik J. Simons<sup>a</sup>

<sup>a</sup>*Department of Geosciences, Princeton University, Princeton, NJ 08540*

<sup>b</sup>*School of Earth Sciences, University of Bristol, Bristol, UK*

---

## Abstract

The eastern continental margin of North America, despite being a passive margin at present, records a comprehensive tectonic history of both mountain building and rifting events. This record is punctuated by several igneous events, including those associated with the Great Meteor and Bermuda hotspots. To gain a better understanding of the state of the mantle beneath this region, we employ the massive quantity of seismic data recorded by the USArray to image the mantle transition zone beneath eastern North America. To construct these images, we first calculate  $P$ -to- $s$  receiver functions using an iterative time-domain deconvolution algorithm. These receiver functions are then automatically filtered by their quality, using a set of rigorous criteria, and subsequently summed using common conversion point stacking. We present several cross sections through these stacks, which show remarkable features such as a thinned transition zone beneath the independently observed northern Appalachian and central Appalachian low-wavespeed anomalies, as well as a thickened transition zone beneath western Tennessee associated with the Laramide slab stagnating at depth. In addition to discussing these geologically relevant features, we perform a technical analysis of the effects of using various seismic velocity models for the moveout correction of our receiver functions. We find that the thickness of the mantle transition zone under eastern North America is a robust measurement, while the resolved depths of the 410 and 660 km discontinuities are model dependent.

*Keywords:* mantle transition zone, receiver functions, Appalachian Mountains, Great Meteor hotspot, Laramide slab

---

## 1. Introduction

To acquaint the reader with the key events that have shaped the geologic history of eastern North America, we briefly review them here. A sensible starting point is the Appalachian orogeny, which occurred roughly 300 Ma during the collision of the African and North American continents (Hatcher et al., 2010).

---

\*Corresponding author, now at RPS Group, a Tetra Tech Company  
*Email address:* [aburky@alumni.princeton.edu](mailto:aburky@alumni.princeton.edu) (Alexander L. Burky)

5 Around 230–200 Ma, the supercontinent of Pangaea broke up, causing eastern North America to rift apart  
6 from Africa (Brunsvik et al., 2021). By about 100 Ma, the Farallon slab was subducting beneath central  
7 North America (Sigloch, 2011), while the Great Meteor hotspot was active beneath New England (Kinney  
8 et al., 2021). Finally, at 50–30 Ma, magmatic activity in the region led to the formation of Bermuda, and  
9 scattered basaltic volcanism in the central Appalachians (Mazza et al., 2014). When we consider all of these  
10 events, it makes sense that eastern North America warrants a special classification as a *volcanic* passive  
11 margin (Geoffroy, 2005).

12 In this work, we employ mantle transition zone (MTZ) receiver functions to map the depths to the 410  
13 and 660 km discontinuities (hereafter referred to as ‘the 410’ and ‘the 660’) beneath eastern North America,  
14 as well as the MTZ thickness in the region. Evidence for a ‘520’ is weak, yet widespread (Zhang et al., 2022).  
15 For a comprehensive review of mantle seismic discontinuities, see Deuss et al. (2013). Recent high-frequency  
16 global studies have revealed significant short-wavelength complexity at the base of the mantle transition  
17 zone (e.g., Wu et al., 2019; Mao et al., 2022). The recent gains in data coverage and the availability of  
18 multiple high-quality tomographic velocity models enable our present investigation into the structure of this  
19 dynamically important zone. Our high-resolution results are made possible by the dense spatial coverage of  
20 data provided by the USArray (Long et al., 2014).

21 Previous receiver function studies using USArray data have observed a variety of features in the MTZ  
22 beneath the eastern United States: notably, thickening beneath the midwest from Iowa to Tennessee (Maguire  
23 et al., 2018) and moderate thinning beneath areas along the Atlantic coastal plain into the Appalachians  
24 (Keifer & Dueker, 2019). These observations agree with an earlier receiver function study which also identified  
25 thinning in the region beneath the central Appalachians and the adjacent Atlantic coastal plains (Li et al.,  
26 1998, their Fig. 3c).

27 In addition to receiver functions, work has been done using *SS* precursors to map the structure of the  
28 MTZ beneath North America. One difficulty with these studies is the reliance on favorable event-station  
29 geometries for *SS* bounce points, leading to poorer resolution than receiver functions beneath the USArray  
30 (Houser, 2016; Huang et al., 2019; Zhang et al., 2023). This problem has only recently begun to be remedied  
31 with methods to use near-station topside reverberations, such as *Ss660s*, which increase the range of usable  
32 geometries for precursor studies (Shearer & Buehler, 2019). Interestingly, the latter study also observed  
33 thickening of the MTZ beneath the Midwest, with a pronounced thickening below western Tennessee. The  
34 thinning beneath the Atlantic coastal plain, however, appears more modest in that study, noting that it lies  
35 at the edge of their resolvable region.

36 Adding to the complexity of our study area is the New Madrid Seismic Zone (NMSZ) beneath eastern  
37 Missouri and western Tennessee, which has been the host of several large earthquakes in recorded history

38 (Page & Hough, 2014). MTZ studies have identified significant thickening beneath the NMSZ, but no link  
39 has been established between these two features (Gao & Liu, 2014). This thickening has, however, been  
40 attributed to a stagnant portion of the Farallon slab, referred to as the Laramide slab, which today resides  
41 in the MTZ (Sigloch, 2011). This feature has been consistently resolved in a  $P$  wave travel-time tomography  
42 study (Wang et al., 2019), and a joint  $P$  and  $S$  wave travel-time tomography study (Savage, 2021).

### 43 *1.1. The Northern Appalachian Anomaly*

44 In the northeastern United States, seismic studies have revealed the presence of a strong, localized,  
45 low-velocity anomaly, which has been hypothesized to be an indication of geologically recent asthenospheric  
46 upwelling 100 to 300 km beneath New England (Menke et al., 2016; Levin et al., 2018). This feature has been  
47 referred to as the Northern Appalachian Anomaly (NAA). Geographically coincident with this feature is the  
48 track of the Great Meteor hotspot (Morgan, 1971), which is thought to have underlain the region from  $\sim$ 140  
49 to 100 Ma (Kinney et al., 2021), but now underlies the Atlantis-Meteor Seamounts (Sleep, 1990) east of the  
50 Mid-Atlantic Ridge. Attributing the present-day seismic velocity anomalies to this long gone hotspot appears  
51 contradictory, and has encouraged authors to propose alternative scenarios such as edge-driven convection  
52 (King & Anderson, 1998), or lithospheric delamination after the Appalachian orogeny some 300 Ma (Nelson,  
53 1992; Levin et al., 2000).

54 A geochemical study by Torgersen et al. (1995) measured excess  $^3\text{He}$  in groundwater in New Hampshire.  
55 Their observations were suggestive of geologically recent contamination by a reservoir containing primordial  
56 mantle helium, which is typical of volcanically active regions such as ocean islands (Jackson et al., 2017)—not  
57 of geologically old and quiescent regions like the northeastern United States. One possible explanation for  
58 this particular signature is that it may be a remnant of the extensive White Mountain plutonism (190–90 Ma)  
59 associated with the passage of the Great Meteor plume.

60 Deeper into the mantle, several recent tomography models have imaged low-velocity anomalies extending  
61 through the MTZ beneath the northeastern United States. Sigloch (2011) refers to these features as the “slow  
62 blanket” above the old Farallon slab, owing to their location directly above an eastward dipping high-velocity  
63 feature beneath the Midwest and eastern North America. A more recent tomography study by Savage (2021)  
64 also imaged low  $V_P$  and  $V_S$  anomalies extending through the MTZ beneath this region. The appearance of  
65 these anomalies directly above the old Farallon slab is not likely to be a coincidence, and some authors have  
66 speculated it may be the signature of a deep de-watering phenomenon (van der Lee et al., 2008).

### 67 *1.2. The Central Appalachian Anomaly*

68 Toward the south, the presence of a roughly linear seismic low-velocity anomaly in the lower lithosphere  
69 extending from Missouri to Virginia has been interpreted as a previously undetected hotspot track (Chu et al.,

2013). This theory is reinforced by the presence of 75-Myr-old diamondiferous kimberlites in Kentucky (Agee et al., 1982), thought to be sourced from a deep mantle reservoir. The timing of these events, however, is inconsistent with Eocene ( $\sim 47$  Ma) basaltic volcanism in this same region (Mazza et al., 2014). This second event is temporally coincident with offshore magmatic activity which led to the formation of Bermuda and its associated large bathymetric swell (Vogt & Jung, 2007), whose origin remains ambiguous (Burky et al., 2021b) due to the lack of an associated hotspot track and geochemical signatures (Mazza et al., 2019).

A study of seismic anisotropy in this region observed null splitting near the Atlantic coast, which the authors interpreted as vertical flow induced by the impinging Farallon slab (Long et al., 2010). These observations are compounded by the presence of high attenuation in the asthenosphere beneath the area, ascribed to upwelling asthenosphere and the possible presence of melt (Byrnes et al., 2019). Seismic tomography models consistently resolve a low-velocity anomaly extending through the upper mantle beneath this region at present (e.g. Simmons et al., 2010, 2012; Schaeffer & Lebedev, 2014; Lei et al., 2020), alluding once again to the presence of a long-gone hotspot. These low-velocity anomalies are so persistent in tomography models that they have been referred to as the Central Appalachian Anomaly (CAA) (Schmandt & Lin, 2014).

## 2. Data & Modeling

Our main data type in this work is the  $P$ -to- $s$  conversion of teleseismic earthquake waves at discontinuities in the mantle. To isolate these converted phases, we first requested three-component seismograms recorded by a subset of USArray stations (network code TA, for Transportable Array) for all earthquakes with a moment magnitude  $M_w > 5.5$  and within an epicentral distance  $35^\circ \leq \Delta \leq 90^\circ$  of the station (see Fig. 1). This resulted in 1,995 events recorded by 702 stations. We then removed the mean and linear trend from each record, and corrected for the instrument response, converting our seismograms from digital counts to velocity (m/s) using the methods outlined by Burky et al. (2021a). Before any subsequent processing, we bandpassed all seismograms between 0.02 and 0.2 Hz using a third-order Butterworth filter. Each record was then cut 30 s before and 90 s after the theoretical  $P$ -wave arrival time calculated in one-dimensional (1-D) seismic velocity model *iasp91* (Kennett & Engdahl, 1991), to create a record containing only the  $P$ -wave and its coda. To maximize  $P$ -to- $s$  converted energy, we rotated the horizontal components from the north and east (NE) orientation to the radial and transverse (RT) orientation.

After performing these preliminary processing steps, we calculated receiver functions by deconvolving the vertical ( $Z$ ) from the radial ( $R$ ) component using the iterative time domain deconvolution algorithm of Ligorria & Ammon (1999), as described and implemented by Burky et al. (2021b). This resulted in 173,801 radial receiver functions. Since we are not focused on investigating anisotropy in this work, we did not



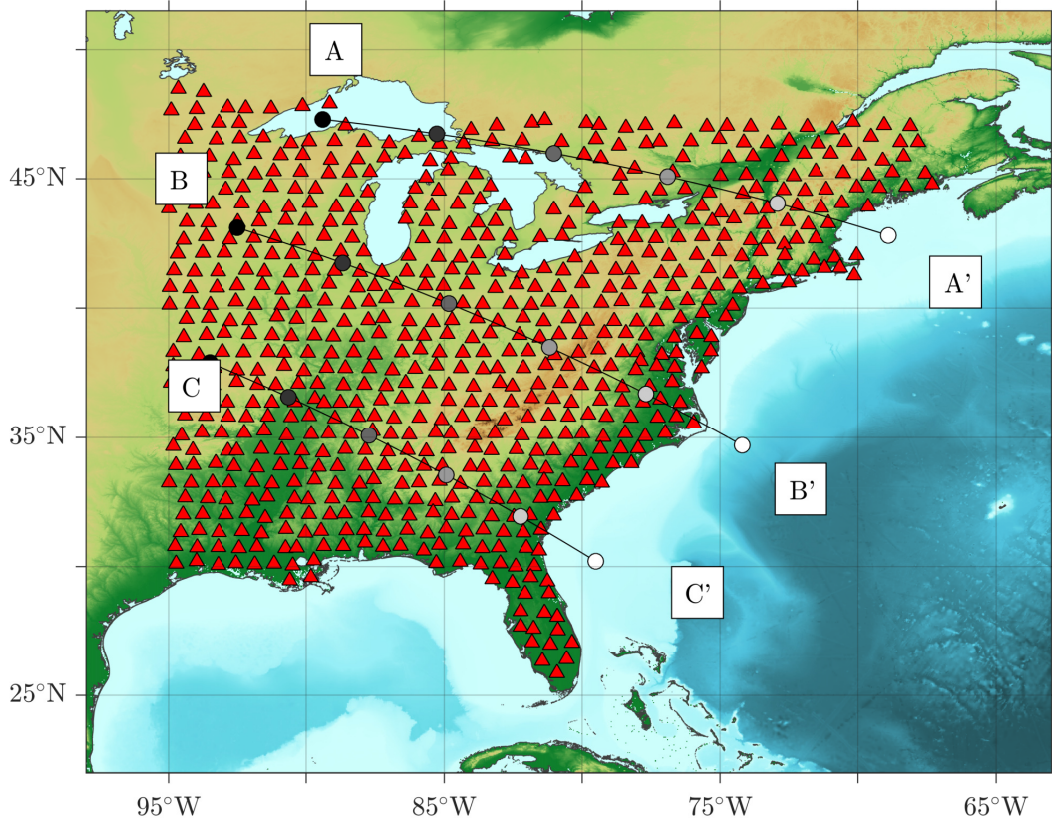


Figure 1: Distribution of the USArray Transportable Array (TA) seismometers (red triangles) which contributed data to our study. Great-circle sections indicate cross sections A-A', B-B', and C-C', which are discussed in the *Results*. The gray dots are intended to act as distance markers along the cross sections. The Great Meteor seamounts are near label A', and the bathymetric swell surrounding Bermuda is east-southeast of label B'. See Supplementary Fig. S1 for an annotated map.

101 compute transverse receiver functions, and our results do not inform us of any differences between  $V_{SV}$  and  
 102  $V_{SH}$  in the study region. Before continuing with any analysis, we performed an automated quality control  
 103 of these receiver functions. The four parameters that we calculate for each receiver function are, (1) the Z  
 104 component signal-to-noise ratio (SNR), (2) the R component SNR, (3) the quality of fit calculated after the  
 105 iterative time domain deconvolution, and (4) a receiver function quality factor,  $\nu$ , quantifying the shape of  
 106 the resulting receiver function (for further details about these four parameters, see Burky et al., 2021b). We  
 107 accepted receiver functions with SNR values greater than 2, quality of fit greater than 80%, and  $\nu$  greater  
 108 than 0.1. After this step, 40,571 receiver functions remained (see Fig. 2 for the geographic distribution of  
 109 the accepted receiver functions). Although our dataset shows a geographic bias in terms of the distribution  
 110 of events, this does not influence any of our interpretations due to the extremely dense station coverage  
 111 provided by the USArray (see Fig. 3).

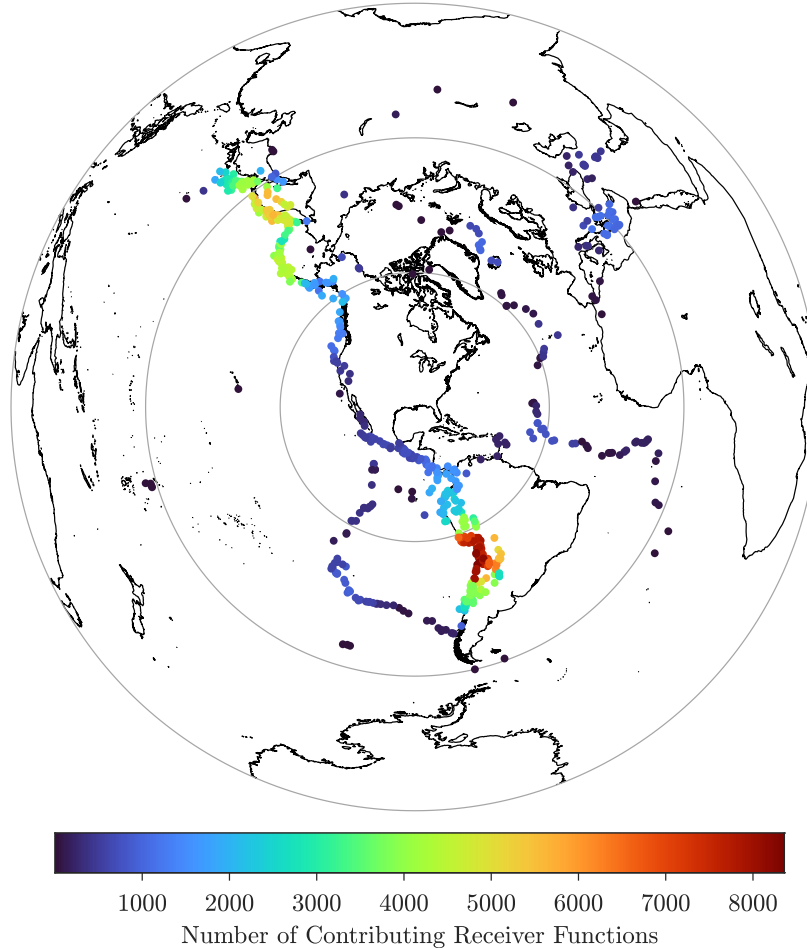


Figure 2: Distribution of the events contributing to the 40,571 high-quality receiver functions used in this study. Each colored dot represents the total number of accepted receiver functions within a  $2^\circ \times 2^\circ$  area around a given event. Concentric gray circles are evenly spaced at distances of  $45^\circ$ , up to a maximum of  $135^\circ$  from the center of the array. Most of our data come from events along the Pacific Ring of Fire, but there are additional contributions from the Mid-Atlantic Ridge and the eastern Mediterranean. Also note that there is considerably more data from distances between  $45^\circ$  and  $90^\circ$  from the center of the array, as events within this distance range are recorded by the majority of stations used in our analysis. Supplementary Fig. S5 shows the depths of these events.

### 112 3. Methods

113 In order to meaningfully analyze and interpret our receiver functions, we performed additional processing  
 114 steps to resolve the mantle transition zone discontinuities that we are concerned with imaging. The first  
 115 of these steps is the moveout correction of our data, allowing us to go from the time domain to the depth  
 116 domain via a seismic velocity model. Then, using these depth-domain receiver functions, we can produce  
 117 images of the desired discontinuities by utilizing stacking techniques. These stacks can then be visualized  
 118 and analyzed to construct maps of the MTZ properties across our study region.

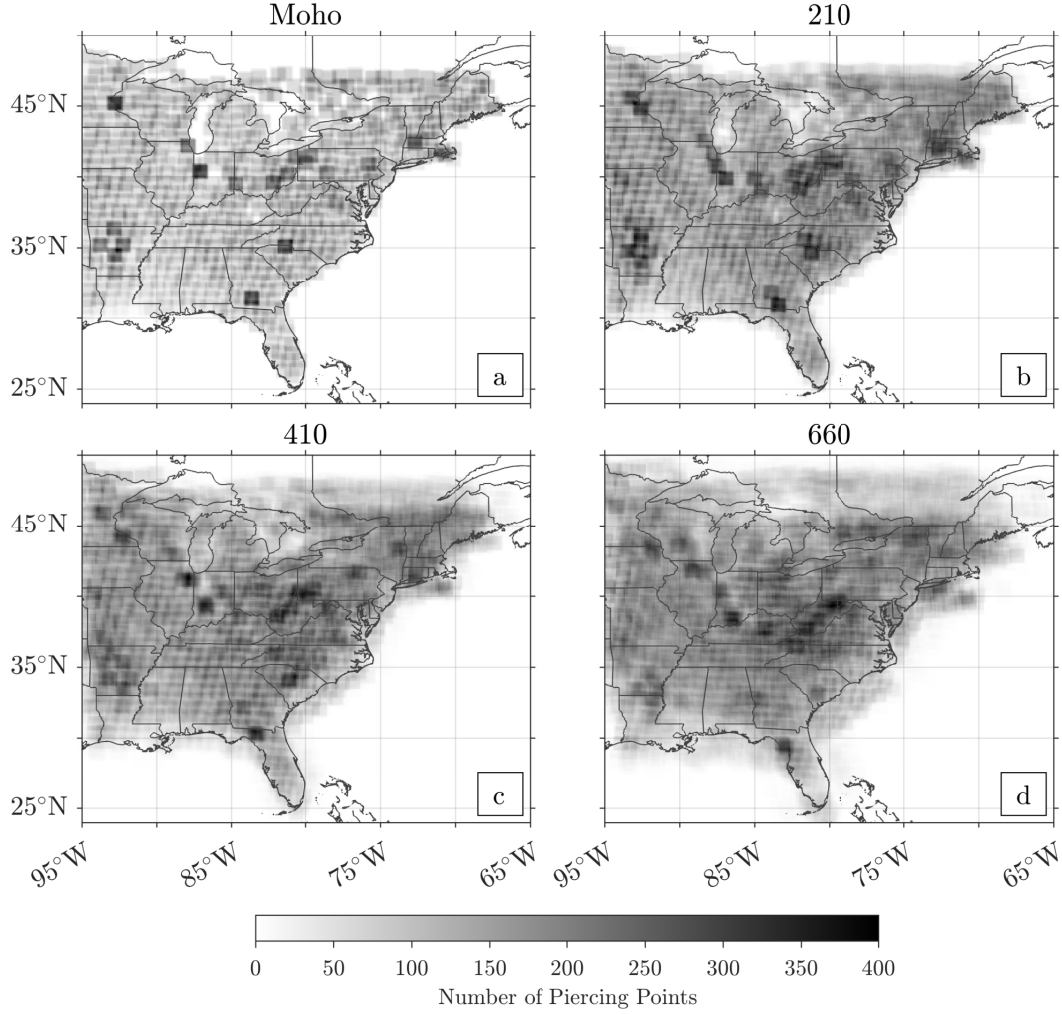


Figure 3: Density of receiver functions contributing to  $1^\circ \times 1^\circ$  cells at four mantle depths (‘Moho’ corresponds to 35 km). Ray coverage is fairly uniform throughout the mantle transition zone, but is biased by the locations of stations at shallower depths. Bins with anomalously high densities of contributing receiver functions can be attributed to exceptional data quality at certain stations, combined with the somewhat uneven spacing of the US Array stations. See Supplementary Fig. S6 for station density.

### 119 3.1. Time to Depth Conversion

120 To accomplish our first task of depth converting the receiver functions, we make use of the following time  
 121 to depth conversion formula (Chevrot et al., 1999):

$$t_{Pds}(p, Z) = \int_0^Z \left[ \sqrt{V_S^{-2}(z) - p^2 r^{-2}} - \sqrt{V_P^{-2}(z) - p^2 r^{-2}} \right] dz, \quad (1)$$

122 where  $t_{Pds}(p, Z)$  is the time in the receiver function corresponding to a conversion from a particular depth,  
 123  $Z$ , in a seismic velocity model with  $P$  and  $S$  wave speeds as a function of depth  $z$ , given by  $V_P(z)$  and  $V_S(z)$ ,  
 124  $p$  is the  $P$ -wave ray parameter (s/km) of the particular event-station pair, and  $r \in [0, 1]$  is the ratio of the

125 discontinuity radius,  $R_{\oplus} - Z$ , to the Earth’s radius,  $R_{\oplus}$ . We compute this integral in six different velocity  
126 models, using a depth increment of  $\Delta z = 0.1$  km.

127 The first model which we used to perform time-to-depth conversion was 1-D reference model *iasp91*  
128 (Kennett & Engdahl, 1991). Next, we used a hybrid 1-D/3-D model made by replacing the crust in *iasp91*  
129 by the 3-D global crustal velocity model CRUST1.0 (Laske et al., 2013). Lastly, we used four different 3-D  
130 tomography models. Three of these models are global models: GyPSuM (Simmons et al., 2010), LLNL\_G3-  
131 D\_JPS (Simmons et al., 2012), and GLADM25 (Lei et al., 2020), and the fourth model is a regional model  
132 of North America, SL2013NA (Schaeffer & Lebedev, 2014). We selected these four tomography models  
133 because they span a range of model construction philosophies, have different sampling densities, and are  
134 publicly available, user-friendly models containing absolute  $P$ - and  $S$ -wave velocities in our study region.  
135 We recognize that there are many more tomography models to choose from that could be used to perform  
136 the time-to-depth conversion, not to mention additional complexity such as wavespeed anisotropy (Chang  
137 et al., 2014). The open-source software that we developed for our study lends itself to reuse by other authors  
138 wishing to investigate the effects of additional tomographic models.

139 To highlight the properties of the four selected tomographic models, we briefly review them here. Model  
140 GyPSuM is constructed largely from body-wave data ( $P$ - and  $S$ -wave traveltimes), with the addition  
141 of gravity, plate motion, dynamic topography, CMB ellipticity, and mineral physics parameters. Model  
142 LLNL\_G3D\_JPS builds on GyPSuM with additional body-wave traveltime measurements, and a more densely  
143 spaced model parameterization. In contrast, global model GLADM25 uses a full-waveform approach on much  
144 longer period data (down to 17 s) to constrain  $P$ - and  $S$ -wave velocities in a transversely isotropic model.  
145 Lastly, regional model SL2013NA inverts surface and  $S$ -waveform data to constrain perturbations in  $P$  and  
146  $S$  velocity and  $S$ -wave azimuthal anisotropy with respect to a reference model based on Crust2.0 (Bassin  
147 et al., 2000) and *ak135* (Kennett et al., 1995). All four of the selected models contain crustal heterogeneity;  
148 however, global model GyPSuM has such low resolution in the crust (on the order of  $5^\circ$ ) that it does not  
149 effectively capture small scale features.

150 In order to use the integral in eq. (1) with these 3-D models, we used the ray-tracing tool of model  
151 LLNL\_G3D\_JPS to compute  $P$ -wave raypaths through that model to find the paths corresponding to each  
152 event-station pair in our dataset. We used these paths for the remaining 3-D models, and we used  $P$ -wave  
153 paths calculated using the TauP-Toolkit (Crotwell et al., 1999) for 1-D model *iasp91* and the hybrid model  
154 that includes CRUST1.0. All of the models were then queried along these respective raytraced paths to  
155 construct the necessary velocity profiles,  $V_P(z)$  and  $V_S(z)$ . It is also worth noting that in our time-to-depth  
156 conversion process we are not accounting for any effects of anisotropy on  $V_S$ . The models we are using  
157 to depth-convert our receiver functions have isotropic  $S$ -wave velocities, so a deviation in  $V_{SV}$  from these

158 velocities would lead to a shift in the absolute depths of discontinuities resolved with this method. Despite  
159 this limitation, as we will show in our *Results* and *Discussion* sections, the resolved absolute depths of MTZ  
160 discontinuities are highly model dependent, while the MTZ thickness is shown to be robust. Since radial  
161 anisotropy is most significant at shallow depths and near subduction zones, and less significant within the  
162 MTZ (e.g. Chang et al., 2015; Simmons et al., 2021), we ignore its effects here.

### 163 3.2. Common Conversion Point Stacking

164 The dense geographic distribution of stations in our dataset allowed us to employ array processing tech-  
165 niques to robustly construct high-resolution images of the MTZ beneath eastern North America. Specifically,  
166 we produced common conversion point (CCP) stacks of our data, inspired by the method outlined by Dueker  
167 & Sheehan (1997). The data density for our CCP stacks is shown in Fig. 3. Our data coverage in the man-  
168 tle transition zone is fairly consistent over the entire study region, and the majority of bins beneath the  
169 continent contain at least 100 receiver functions.

170 First, we calculated theoretical raypaths through 1-D model *iasp91* for all of our event-station pairs  
171 using the TauP Toolkit. Next, we constructed a grid containing the latitude range  $22.5^{\circ}\text{N}$  to  $51.5^{\circ}\text{N}$ , and  
172 the longitude range  $98.5^{\circ}\text{W}$  to  $63.5^{\circ}\text{W}$ , with a  $1^{\circ} \times 1^{\circ}$  cell size. We then found where the computed raypaths  
173 pierced our grid at depths 35, 210, 410 and 660 km. Depth-converted receiver functions corresponding to  
174 each of these rays were then stacked together with the other rays which were contained in the  $1^{\circ} \times 1^{\circ}$  cell,  
175 to create a volume where the center of each cell contained a CCP-stacked receiver function. The entire grid  
176 was then shifted sequentially by increments of  $0.1^{\circ}$ , and the stacking was repeated, until the grid had been  
177 shifted by  $1^{\circ}$ . This resulted in a volume with CCP stacks of  $1^{\circ} \times 1^{\circ}$  stacking width on a grid of resolution  
178  $0.1^{\circ} \times 0.1^{\circ}$ . Finally, the CCP volumes containing each of our four chosen piercing depths (35 km, 210 km,  
179 410 km, and 660 km) were stitched together to construct our final CCP volume, where the depth range  
180 0—120 km corresponds to the 35 km stack, 120—300 km corresponds to the 210 km stack, 300—530 km to  
181 the 410 km stack, and 530—750 km to the 660 km stack (the stitched joins can be seen in the cross-section  
182 slices shown in Figs. 4–6).

## 183 4. Results

184 After computing the common conversion point stacks as described above, we have at our disposal a  
185 collection of six different images of the mantle transition zone beneath eastern North America. Using these  
186 stacks, we can seek answers to two important questions: first, what is the effect of the choice of seismic  
187 velocity model on the resulting image? And second, are there specific features of the MTZ discontinuity  
188 structure which are clearly and commonly resolved in each of our CCP stacks?

189 In an effort to answer the first question, we start by visually comparing a sequence of cross sections  
190 taken through each of our CCP stacks. Selected cross sections can be found in Figs. 4, 5, and 6. The first  
191 point to note is that we clearly resolve both the 410 and 660 in each of these cross sections, regardless of  
192 the velocity model used to moveout-correct our receiver functions. Second, the average amplitude of the 410  
193 signal tends to be higher than that of the 660 signal (see Supplementary Fig. S11). This difference could  
194 indicate that the magnitude of the  $S$ -wave velocity contrast at the 660 is weaker than that at the 410. A  
195 thorough investigation quantifying the magnitude of this difference is beyond the scope of this study and may  
196 require consideration full-waveform effects (Zhang et al., 2023). Another factor leading to this amplitude  
197 difference could be due to the fact that the time-depth conversion, eq. 1, becomes less accurate for converted  
198 waves at this depth, as can be seen by the slightly underestimated depth of the 660 (see Fig. S7), leading  
199 to less constructive stacking of signals from the 660. The third result to note is that each of the selected  
200 cross sections displays a considerable amount of topography on the MTZ discontinuities, as we explore more  
201 fully below. Finally, the resulting images seem to resolve consistent features regardless of the velocity model  
202 used, but with relative shifts in the depths of the discontinuities. These discrepancies are likely due to the  
203 differences in model construction (data types, inversion methods) described above, leading to a range of  $Pds$   
204 moveouts across different models.

205 To further explore this final point, we performed pairwise cross correlations between each of our CCP  
206 stacks, in an effort to see how consistent the resolved features were. We found that our stacks were strongly  
207 correlated with one another (correlation coefficient  $\rho > 0.9$ ) with relative shifts of about 10–20 km. Ani-  
208 mations showing these cross correlations across the entire CCP volume can be found in the Supplementary  
209 Materials, and stills from these animations are included as Supplementary Figs. S15–S21. To our knowledge,  
210 this is the first analysis of the pairwise cross correlations of a suite of CCP stacked receiver functions. These  
211 animations show that the choice of velocity model used in depth converting receiver functions can lead to  
212 large variations in the resulting depths of the 410 and 660. However, these variations tend to shift both  
213 discontinuities in the same direction, implying that the measured thickness of the mantle transition zone is  
214 less sensitive to the choice of velocity model.

215 To help illustrate this point, as well as to explore the geographic variations in MTZ discontinuity structure,  
216 we made maps showing the depths of the 410 and 660, as well as the measured MTZ thickness, in all of  
217 our 3-D corrected CCP stacks (see Fig. 7). In these maps, we can see that model GLADM25 tends to  
218 shift the 410 and 660 to greater depths, while model SL2013NA tends to shift them to shallower depths.  
219 Models GyPSuM and LLNL\_G3-D\_JPS show less exaggerated shifts of the discontinuities away from 410 and  
220 660 km. All four models, however, show a relatively thinned region east of the Appalachians, compared to  
221 the global average of 242 km (Lawrence & Shearer, 2006), and a relatively thickened region to the west of

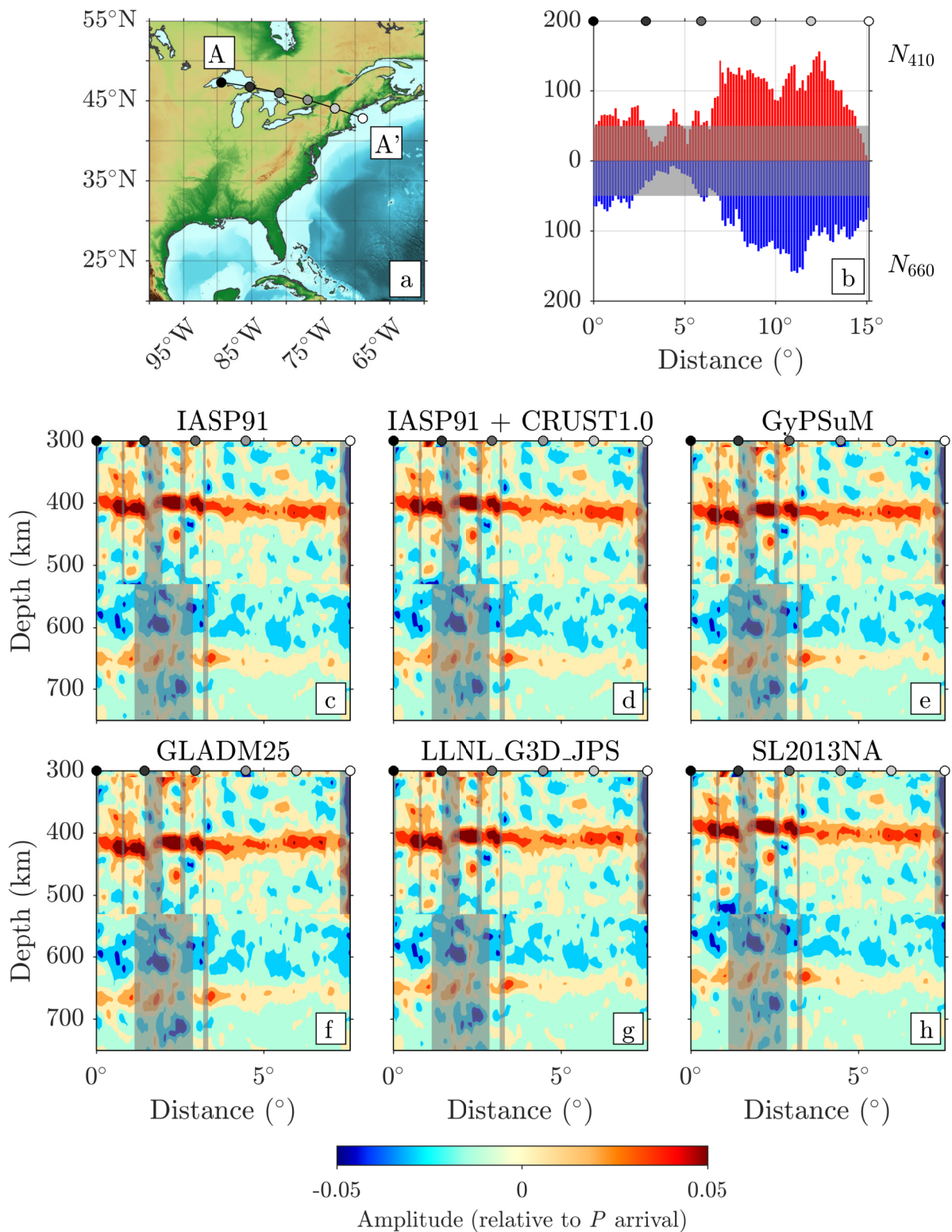


Figure 4: Mantle transition zone (MTZ) structure in the region of the Northern Appalachian Anomaly (NAA). (a) Map showing the location of the cross section. (b) Histogram showing the number of receiver functions contributing to the 410 (red) and 660 (blue) portions in the cross section. Data quantity tapers off near the Great Lakes and into Canada. (c-h) Cross sections through common conversion point (CCP) stacks in six different tomographic velocity models described in *Methods*. Bins with fewer than 50 receiver functions are covered with a transparent gray box, corresponding to the grayed-out region of panel (b). Note the relative thinning of the MTZ from NW to SE along this cross section, coincident with the location of the NAA.



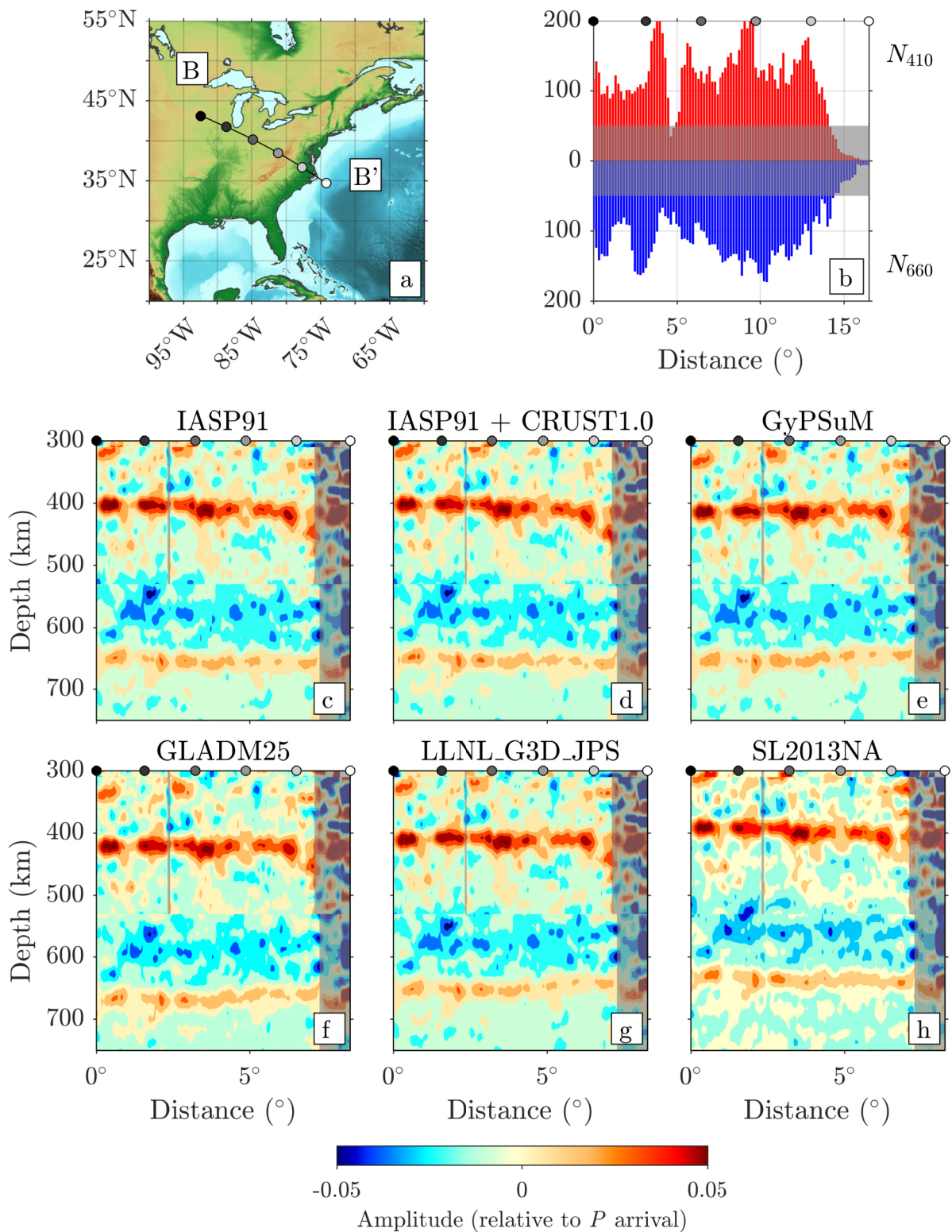


Figure 5: Mantle transition zone (MTZ) structure in the region of the Central Appalachian Anomaly (CAA), laid out as Fig. 4. Note the considerable amount of topography on the 410 discontinuity, and the strong thinning of the MTZ at the SE end of the cross section. Also note the data sparsity and poor resolution at the southeasternmost end of this cross section. The negative-polarity signals around 600 km depth (also present in Figs. 4 and 6), despite having a similar magnitude to  $P660s$ , are most likely artifacts from filtering (see Supplementary Fig. S7) and the presence of the  $PcP$  phase.



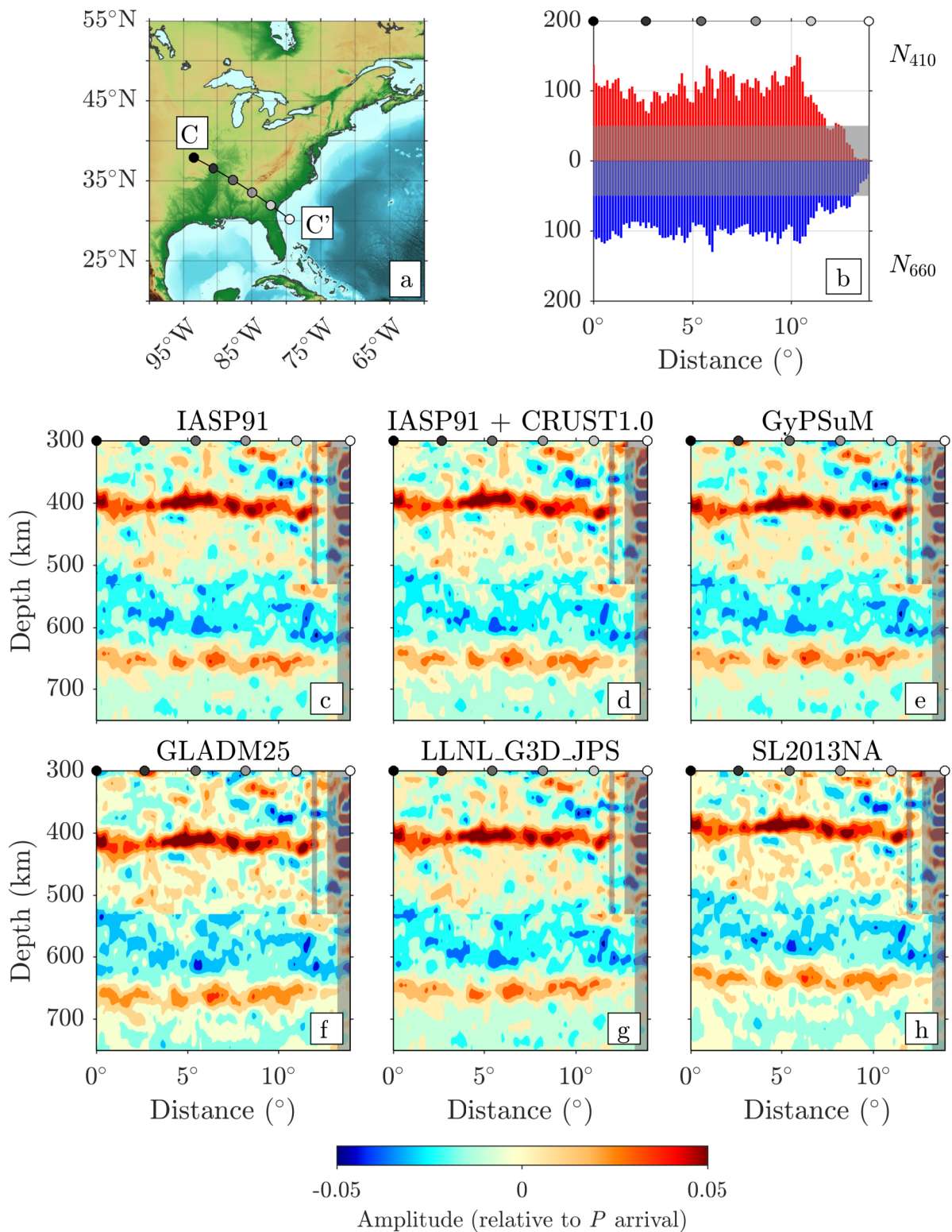


Figure 6: Mantle transition zone (MTZ) structure in the region of the Southern Appalachian Anomaly, laid out as Fig. 4. Note again the strong topography on the 410 and 660 discontinuities. This cross section shows significant thickening of the MTZ at the western end of the cross section, beneath western Tennessee. Data coverage is fairly uniform, with resolution tapering off at the southeasternmost end of this cross section.

222 the Appalachians. Of particular interest are two roughly linear thinned zones which trend NW-SE. These  
223 thinned zones correspond to cross sections A-A', B-B' (see Figs. 4 and 5). In addition, a thickened region  
224 beneath western Tennessee is manifest in cross section C-C' (see Fig. 6).

## 225 5. Discussion

### 226 5.1. *The Importance of 3-D Moveout Corrections*

227 We have shown that the choice of seismic velocity model has a considerable effect on the apparent depth  
228 of the MTZ discontinuities. In the most extreme case, an average discrepancy of 21.6 km in the apparent  
229 depth of the 410 and an average discrepancy of 26.1 km in the apparent depth of the 660 were found between  
230 CCP stacks made using models GLADM25 and SL2013NA (see Supplementary Figs. S9 and S10). These  
231 discrepancies are contrasted by an average difference of 4.4 km between the apparent MTZ thicknesses found  
232 in these stacks (see Fig. 8). This highlights that the apparent depths of the 410 and the 660 can be difficult  
233 to accurately constrain using receiver functions, even after performing 3-D depth corrections. Fortunately,  
234 the MTZ thickness is much more consistently resolved regardless of the seismic velocity model used to depth  
235 convert receiver functions. Consequently, this is the feature which we will frame our discussion on, and we  
236 suggest that future MTZ receiver function studies follow this example.

237 In an effort to explore and understand the mechanism leading to these discrepancies, we performed an  
238 analysis of the time-to-depth conversion integral in Eq. 1 for each of the 3-D velocity models used in our  
239 study. The results of this analysis are summarized in Supplementary Fig. S8. We found that the *Pds*  
240 conversion depth associated with a particular time in a receiver function varied considerably from the outset  
241 in each of the 3-D models. For times in the range of 0 to 10 s after the *P* arrival in the receiver function,  
242 there is a spread in possible conversion depths of roughly 4 km. This would lead to relative discrepancies  
243 in apparent Moho depths on the order of 4 km. At times greater than 20 s, this discrepancy has grown to  
244 roughly 20 km, as can be seen in our results. The slopes of these curves, however, remain roughly constant  
245 through the times associated with MTZ *Pds* arrivals, which leads to the decreased variability in our observed  
246 MTZ thicknesses using different tomographic models.

### 247 5.2. *The Northern Appalachian Anomaly*

248 In light of the previous discussion, we are confident that the observed MTZ thinning in our CCP stacks  
249 is a robust feature. This leads to interesting implications for the NAA, which had only been observed at  
250 shallower asthenospheric depths of 100 to 300 km (Menke et al., 2016; Levin et al., 2018). We suggest  
251 that this feature extends deeper than previously known, and may be associated with a surviving hot thermal

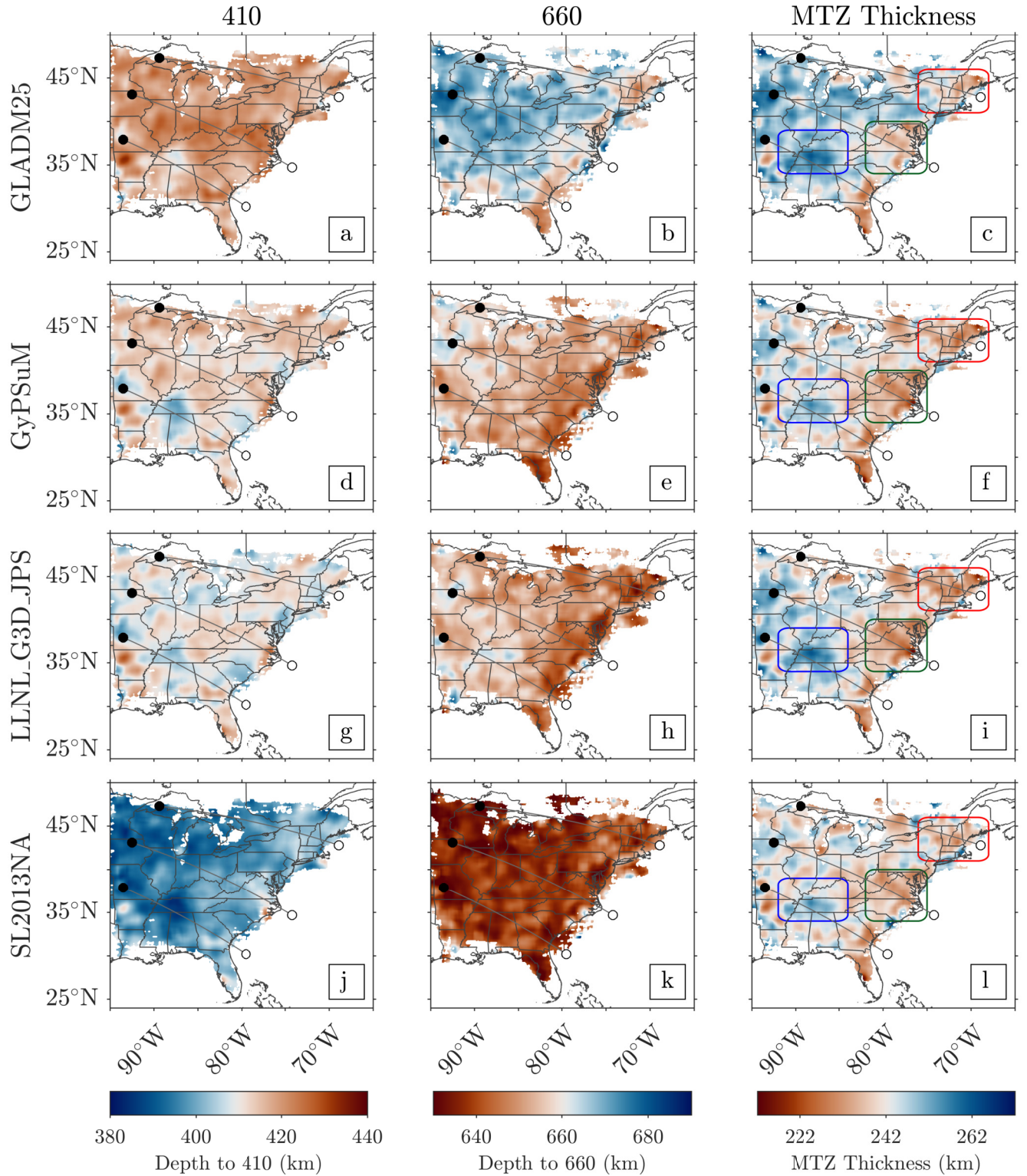


Figure 7: Measured 410 and 660 depth, and MTZ thickness, for CCP stacks made using four different 3-D velocity models for the depth conversion of our receiver functions: (a-c) GLADM25, (d-f) GyPSuM, (g-i) LLNL\_G3D\_JPS, and (j-l) SL2013NA. Only locations with 50 or more receiver functions are shown. Note that models GLADM25 and SL2013NA differ markedly in the depths of the 410 and 660, while GyPSuM and LLNL\_G3D\_JPS seem more consistent with one another. Also note that all four models are fairly consistent in their resolved MTZ thickness. The thinned zones shown in cross sections A-A', B-B', and C-C' (Figs. 4, 5, and 6) are also apparent in all four models. Red, green, and blue inset boxes denote the approximate locations of the NAA, CAA, and Laramide Slab Anomaly, respectively.



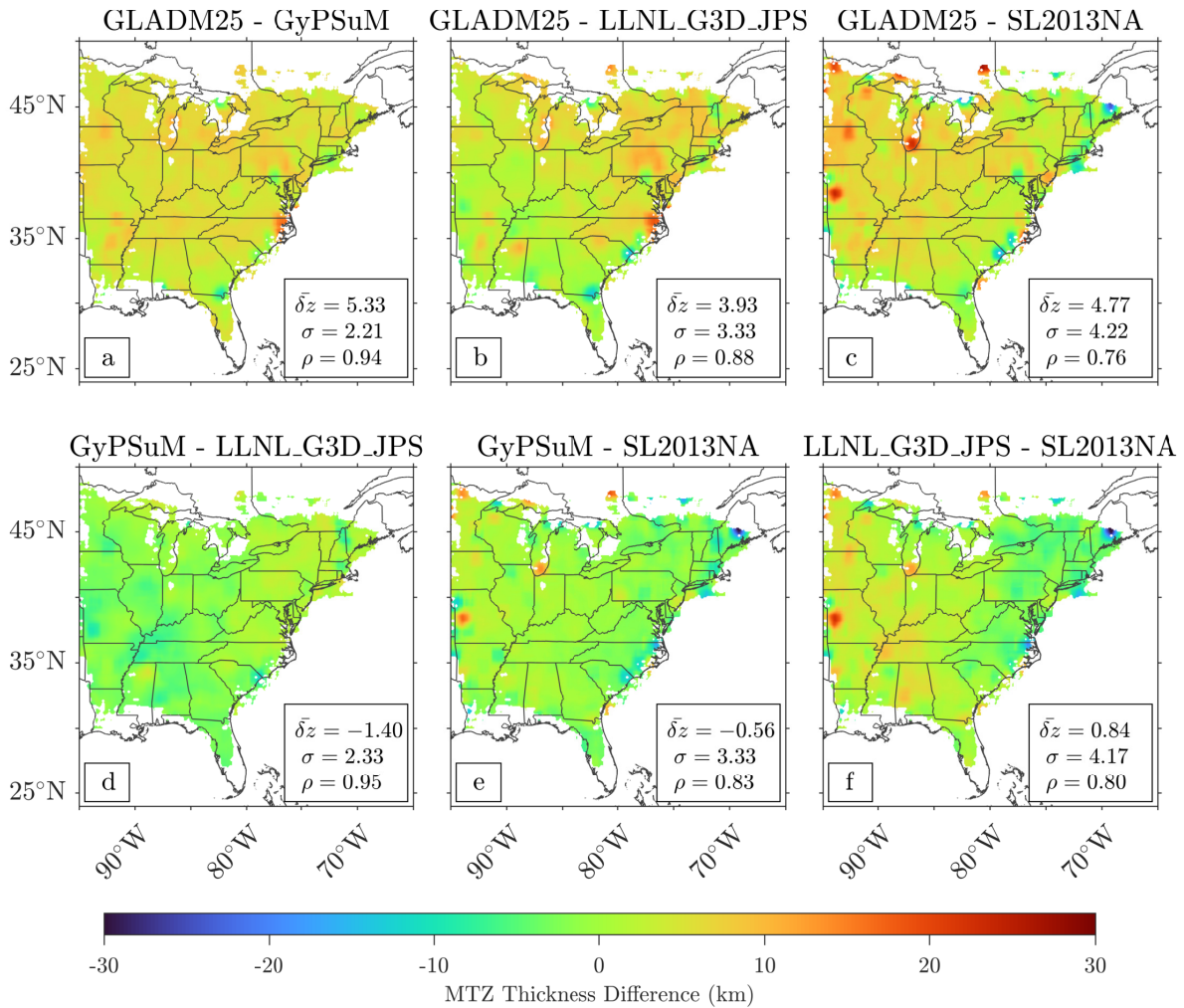


Figure 8: Maps showing the differences between pairs of each of the MTZ thickness maps in Fig. 7. The legends report  $\bar{\delta z}$ , the mean value of the difference,  $\sigma$ , the standard deviation of the difference, and  $\rho$ , the correlation coefficient between the two maps. Note that the differences in thickness are on the order of a few km, and that the maps tend to be well correlated ( $\rho > 0.7$ ). For similar maps showing the differences for the 410 and the 660, see Supplementary Figs. S9 and S10.

252 anomaly beneath New England. See Supplementary Fig. S12 for cross sections through the four tomographic  
 253 velocity models.

254 We can estimate the magnitude of this thermal anomaly using the following relation from Helffrich (2000):

$$z = z_0 + \delta T \left( \frac{dz}{dP} \right) \left[ \left( \frac{dP}{dT} \right)_{660} - \left( \frac{dP}{dT} \right)_{410} \right], \quad (2)$$

255 where  $z$  represents the observed MTZ thickness,  $(dP/dT)_{660}$  and  $(dP/dT)_{410}$  are the Clapeyron slopes of  
 256 the ringwoodite to bridgmanite and magnesiowüstite (ferropericlase) phase transition, and the olivine to  
 257 wadsleyite phase transition, respectively. We use a value of  $z_0 = 242$  km (Lawrence & Shearer, 2006) for

258 the global average MTZ thickness, and values of  $(dP/dT)_{660} = -2.6$  MPa/K and  $(dP/dT)_{410} = 3.1$  MPa/K  
259 (Akaogi et al., 2007) for the Clapeyron slopes. In reality, the Clapeyron slopes of these phase transitions are  
260 somewhat variable, ranging from  $-0.2$  to  $-3.6$  MPa/K for  $(dP/dT)_{660}$  (e.g., Kojitani et al., 2016; Muir et al.,  
261 2021), and  $1.8$  to  $4.0$  MPa/K for  $(dP/dT)_{410}$  (e.g., Yu et al., 2008) due to both experimental uncertainty and  
262 the degree of hydration of the mineral assemblage. However, since  $(dP/dT)_{660}$  is negative and  $(dP/dT)_{410}$  is  
263 positive, the association of a thin transition zone with a positive thermal anomaly holds true. To simplify the  
264 following discussion, we will quote temperature anomalies calculated using the aforementioned Clapeyron  
265 slopes, but the reader should keep in mind that these estimated anomalies could vary by roughly one order  
266 of magnitude with the choice of alternative Clapeyron slope values.

267 Using our four different CCP stacks, we can estimate bounds on the thermal anomaly associated with  
268 the NAA. The minimum MTZ thickness observed in our four models is 223 km (model LLNL-G3-D-JPS,  
269 beneath southern New Hampshire), but there is a range of 6 km in this measurement across the models  
270 (229 km for model GLADM25, see Supplementary Fig. S2 and Table S1). Inserting these values into Eq. 2  
271 gives a range for the maximum thermal anomaly of  $\sim 89$ – $130$  K relative to global average MTZ temperature.  
272 To investigate the significance of this anomaly, we report statistics of the NAA sub-region relative to our  
273 entire dataset (see Table S1). We found that the average MTZ thickness within the NAA was between 235  
274 and 238 km for the four models we tested, corresponding to a modest, positive (warm) thermal anomaly of  
275  $\sim 27$ – $48$  K relative to the global average (Eq. 2). This thickness is roughly one standard deviation thinner  
276 than the average for our entire dataset.

277 Previous receiver function research on the MTZ beneath the NAA reported no evidence of thinning or  
278 deflection of the discontinuities (Li et al., 1998, their Fig. 3c), despite finding modest thinning beneath the  
279 central Appalachians and the adjacent Atlantic coastal plain. This has led recent work to suggest that this  
280 feature does not penetrate through the MTZ, and is instead confined to the shallow asthenosphere at depths  
281 less than 400 km (Menke et al., 2016). Our findings do not invalidate this previous work, but instead build  
282 upon it by suggesting that the NAA may weakly penetrate the MTZ below. In fact, if we consider the  
283 MTZ to be the lowermost extent of a shallow edge-driven convective cell, the observations of W-E aligned  
284 anisotropy can be interpreted as the horizontal flow associated with the bottom of such a cell (Long et al.,  
285 2016; Levin et al., 2018). This could reconcile the puzzling observations of null splitting and W-E anisotropy  
286 beneath the NAA which stand as outliers to the rest of northeastern North America.

### 287 5.3. The Central Appalachian Anomaly

288 We can apply a similar analysis to the anomalously thin MTZ corresponding to the CAA to get an  
289 estimate of the magnitude of its thermal signature. See Supplementary Fig. S13 for cross sections through  
290 the tomographic velocity models.

291 The *minimum* MTZ thickness we observe is 214 km (model LLNL\_G3-D\_JPS beneath the North Carolina-  
292 Virginia border), but there is a range of 14 km across the four models (228 km in models GLADM25 and  
293 SL2013NA, see Supplementary Fig. S3, and Table S1). This yields a range of  $\sim 96$ – $192$  K for the *maximum*  
294 thermal anomaly relative to global average MTZ temperature. When we instead consider the *average* MTZ  
295 thickness within the CAA, we find that it is of similar thickness to the NAA, between 236 and 238 km,  
296 corresponding to an *average* thermal anomaly of  $\sim 27$ – $42$  K relative to the global average.

297 When we consider all of the information presented so far, the CAA and NAA seem to be very similar  
298 in terms of their observed features. Both locations have a record of igneous activity, Eocene ( $\sim 47$  Ma)  
299 volcanism in the area of the CAA (Mazza et al., 2014), and Cretaceous ( $\sim 140$  to 100 Ma) volcanism in  
300 the area of the NAA (Kinney et al., 2021), and the present-day MTZ anomalies are of nearly identical  
301 magnitudes. We suggest that both of these features may be associated with small-scale convective cells  
302 generated by the contrast with the nearby Farallon slab remnants and continental craton. These cells seem  
303 to be long-lived, and may have been present during the passage of both the Great Meteor and Bermuda  
304 hotspots, providing them with the additional heat and buoyancy required to initiate active volcanism and  
305 plutonism. This interpretation is consistent with null splitting observations in both regions (Long et al.,  
306 2016), and with an edge-driven convection model (King & Anderson, 1998). With the passage of another  
307 transient heat source these regions might become active once again.

### 308 5.4. MTZ Thickening Associated with the Laramide Slab

309 In addition to resolving regions of thinned MTZ beneath the NAA and CAA, we observe modest topogra-  
310 phy and thickening of the MTZ west of the Appalachians. Of particular note is a significantly thickened patch  
311 beneath western Tennessee, which we argue is associated with the stagnant Laramide slab. The Laramide  
312 slab is not an entire, distinct slab, but is rather the expression of a period of shallow-angle subduction  
313 of the Farallon slab which occurred 80 to 60 Ma (Humphreys et al., 2015). This shallow subduction was  
314 terminated by a break-off at depth and a westward migration of the trench around 50 Ma (Sigloch et al.,  
315 2008), leaving the shallowly subducting slab stalled in the transition zone. Recent tomographic images sup-  
316 port this interpretation, showing evidence of shallow ( $< 700$  km) seismically fast anomalies in the transition  
317 zone beneath the Midwest (Sigloch, 2011). In the model of Sigloch (2011), these anomalies are greatest in

318 the MTZ beneath western Tennessee, consistent with our observations of maximum thickening there. See  
319 Supplementary Fig. S14 for tomographic cross sections.

320 To quantify the magnitude of the thermal anomaly associated with this relict slab, we measure the  
321 *maximum* MTZ thickness beneath this region (see Supplementary Fig. S4 and Table S1). We observe a  
322 *maximum* MTZ thickness of 263 km (beneath western Tennessee in model GLADM25), and a range of 6 km  
323 for the maximum thickness (257 km in models GyPSuM and SL2013NA). These values correspond to a  
324 range of about  $-103$  K to  $-144$  K for the *maximum* cold thermal anomaly relative to global average MTZ  
325 temperature. When we instead consider the *average* MTZ thickness within this anomaly, we find that it  
326 spans a range of 245 to 249 km, and corresponds to an *average* thermal anomaly of about  $-21$  K to  $-48$  K  
327 relative to the global average. These anomalies are smaller than those observed beneath active subduction  
328 zones at present (van Stiphout et al., 2019), but this is not surprising considering how long the Laramide  
329 slab has been stalled in the MTZ.

### 330 5.5. Synthesis with Previously Published Results

331 As was stated in the *Introduction*, eastern North America is aptly classified as a *volcanic* passive margin  
332 (Geoffroy, 2005). Our results reinforce this classification by demonstrating the plausibility of hot thermal  
333 anomalies in the MTZ beneath the northern and central Appalachian mountains. This result also agrees  
334 with the recent receiver function work by Keifer & Dueker (2019), who found similar thinning beneath  
335 the Appalachians, as well as thickening beneath western Tennessee. The agreement between our studies is  
336 particularly encouraging since for the migration of their receiver functions they used two entirely different  
337 tomography models (Schmandt & Lin, 2014; Golos et al., 2018) than the four we investigated here. Inter-  
338 estingly, the magnitudes of the temperature anomalies they inferred, on the order of  $\pm 300$  K to  $\pm 600$  K,  
339 were even larger than the ones we measured, further emphasizing that the MTZ beneath this region is any-  
340 thing but average. Circling back to the *Introduction*, our results show that despite the lack of any modern  
341 volcanism, the perplexing presence of “hot-spot” signatures such as excess  $^3\text{He}$  in the groundwater in New  
342 Hampshire (Torgersen et al., 1995) can be seen as the dying breaths of the region’s volcanic legacy. The  
343 combination of an incoming slab from the west, the possibility of edge-driven convection to the east, and  
344 intermittent deep-mantle plumes, leaves a remarkable tectonic signature in the MTZ beneath eastern North  
345 America.

## 346 6. Conclusion

347 We have performed an extensive analysis of the structure of the mantle transition zone (MTZ) beneath  
348 eastern North America, and developed and provided a methodological approach by which to do so. Specif-

ically, we have found that the choice of velocity model used to depth-convert receiver functions can lead to significant variations in the observed depths of the 410 and 660 km discontinuities. The overall MTZ thickness, however, is found to be less sensitive to the differences in velocity models, and is therefore a robust feature when it comes to interpreting receiver function results in their respective geologic and geodynamic contexts. With this in mind, we explored a variety of significant features in our dataset: notably, the Northern Appalachian Anomaly (NAA), the Central Appalachian Anomaly (CAA), and Laramide slab anomaly. These features correspond to positive and negative thermal anomalies on the order of  $\pm 100$  K, which may seem modest beneath an active margin or mantle plume, but are noteworthy considering the current status of the region as a passive “volcanic” margin. These observations enhance our understanding of the NAA and CAA, suggesting that they may penetrate into the MTZ instead of being solely confined to shallow asthenospheric depths. Our observations of the stagnant Laramide slab provide additional evidence for slabs stalling in the MTZ, and reinforce the theory of two-stage subduction of the Farallon slab.

## Acknowledgments

The computer code developed for this work, `rflexa` (Burky et al., 2021a), is available online at: <https://github.com/alexburky/rflexa>. We acknowledge the use of the Seismic Analysis Code (SAC) Version 101.6a (Goldstein & Snoke, 2005). Data for this study were provided by the IRIS DMC (doi: 10.7914/SN/TA). This work was partly supported by the U.S. National Science Foundation (NSF) under grants EAR-1736046 and OCE-1917085, and by Princeton University. High-performance computing resources were provided by the Princeton Institute for Computational Science & Engineering (PICSciE). We would like to thank Vadim Levin and Blair Schoene for helpful feedback on the manuscript, as well as Ana Ferreira and three anonymous reviewers who helped to greatly improve the quality of this study.

## References

- Agee, J. J., Garrison, J. R., & Taylor, L. A. (1982). Petrogenesis of oxide minerals in kimberlite, Elliott County, Kentucky. *Am. Mineral.*, *67*, 28–42.
- Akaogi, M., Takayama, H., Kojitani, H., Kawaji, H., & Atake, T. (2007). Low-temperature heat capacities, entropies and enthalpies of  $\text{Mg}_2\text{SiO}_4$  polymorphs, and  $\alpha$ - $\beta$ - $\gamma$  and post-spinel phase relations at high pressure. *Phys. Chem. Miner.*, *34*, 169–183, doi: 10.1007/s00269-006-0137-3.
- Bassin, C., Laske, G., & Masters, G. (2000). The current limits of resolution for surface wave tomography in North America. *Eos Trans. AGU*, *81*, F897.
- Brunsvik, B. R., Eilon, Z. C., & Lynner, C. (2021). Mantle structure and flow across the continent-ocean transition of the eastern North American margin: Anisotropic  $S$ -wave tomography. *Geochem. Geophys. Geosys.*, *22*, e2021GC010084, doi: 10.1029/2021GC010084.
- Burky, A. L., Irving, J. C. E., & Simons, F. J. (2021a). Instrument response removal and the 2020  $M_{Lg}$  3.1 Marlboro, New Jersey, earthquake. *Seismol. Res. Lett.*, *92*, 3865–3872, doi: 10.1785/0220210118.
- Burky, A. L., Irving, J. C. E., & Simons, F. J. (2021b). Mantle transition zone receiver functions for Bermuda: Automation, quality control, and interpretation. *J. Geophys. Res.*, *126*, e2020JB020177, doi: 10.1029/2020JB020177.



- 386 Byrnes, J. S., Bezada, M., Long, M. D., & Benoit, M. H. (2019). Thin lithosphere beneath the  
387 central Appalachian Mountains: Constraints from seismic attenuation beneath the MAGIC array.  
388 *Earth Planet. Sci. Lett.*, *519*, 297–307, doi: 10.1016/j.epsl.2019.04.045.
- 389 Chang, S.-J., Ferreira, A. M. G., Ritsema, J., van Heijst, H. J., & Woodhouse, J. H. (2014). Global  
390 radially anisotropic mantle structure from multiple datasets: A review, current challenges, and outlook.  
391 *Tectonophysics*, *617*, 1–19, doi: 10.1016/j.tecto.2014.01.033.
- 392 Chang, S.-J., Ferreira, A. M. G., Ritsema, J., van Heijst, H. J., & Woodhouse, J. H. (2015). Joint inversion  
393 for global isotropic and radially anisotropic mantle structure including crustal thickness perturbations.  
394 *J. Geophys. Res.*, *120*, 4278–4300, doi: 10.1002/2014JB011824.
- 395 Chevrot, S., Vinnik, L., & Montagner, J.-P. (1999). Global scale analysis of mantle *Pds* phases. *J. Geo-*  
396 *phys. Res.*, *104*, 20203–20219, doi: 10.1029/1999JB900087.
- 397 Chu, R., Leng, W., Helmberger, D. V., & Gurnis, M. (2013). Hidden hotspot track beneath the eastern  
398 United States. *Nature Geosci.*, *6*, 963–966, doi: 10.1038/ngeo1949.
- 399 Crotwell, H. P., Owens, T. J., & Ritsema, J. (1999). The TauP Toolkit: Flexible seismic travel-time and  
400 ray-path utilities. *Geophys. Res. Lett.*, *70*, 154–160, doi: 10.1785/gssrl.70.2.154.
- 401 Deuss, A., Andrews, J., & Day, E. (2013). Seismic observations of mantle discontinuities and their miner-  
402 alogical and dynamical interpretation. In S.-I. Karato (Ed.), *Physics and Chemistry of the Deep Earth*  
403 chapter 10. (pp. 295–323, doi: 10.1002/9781118529492.ch10). New York: John Wiley.
- 404 Dueker, K. G., & Sheehan, A. F. (1997). Mantle discontinuity structure from midpoint stacks of con-  
405 verted *P* to *S* waves across the Yellowstone hotspot track. *J. Geophys. Res.*, *102*, 8313–8327, doi:  
406 10.1029/96JB03857.
- 407 Gao, S. S., & Liu, K. H. (2014). Mantle transition zone discontinuities beneath the contiguous United States.  
408 *J. Geophys. Res.*, *119*, 6452–6468, doi: 10.1002/2014JB011253.
- 409 Geoffroy, L. (2005). Volcanic passive margins. *C. R. Geosci.*, *337*, 1395–1408, doi: 10.1016/j.crte.2005.10.006.
- 410 Goldstein, P., & Snoke, A. (2005). SAC availability for the IRIS community. *Incorporated Research Institu-*  
411 *tions for Seismology Newsletter*, *7*.
- 412 Golos, E. M., Fang, H., Yao, H., Zhang, H., Burdick, S., Vernon, F., Schaeffer, A., Lebedev, S., & van der  
413 Hilst, R. D. (2018). Shear wave tomography beneath the United States using a joint inversion of surface  
414 and body waves. *J. Geophys. Res.*, *123*, 5169–5189, doi: 10.1029/2017JB014894.
- 415 Hatcher, R. D., Tollo, R. P., Bartholomew, M. J., Hibbard, J. P., & Karabinos, P. M. (2010). The Appalachian  
416 orogen: A brief summary. *From Rodinia to Pangea: The Lithotectonic Record of the Appalachian Region:*  
417 *Geological Society of America Memoir*, *206*, 1–19, doi: 10.1130/2010.1206(01).
- 418 Helffrich, G. R. (2000). Topography of the transition zone seismic discontinuities. *Rev. Geophys.*, *38*,  
419 141–158, doi: 10.1029/1999RG000060.
- 420 Houser, C. (2016). Global seismic data reveal little water in the mantle transition zone.  
421 *Earth Planet. Sci. Lett.*, *448*, 94–101, doi: 10.1016/j.epsl.2016.04.018.
- 422 Huang, Q., Schmerr, N., Waszek, L., & Beghein, C. (2019). Constraints on seismic anisotropy in  
423 the mantle transition zone from long-period *SS* precursors. *J. Geophys. Res.*, *124*, 6779–6800, doi:  
424 10.1029/2019JB017307.
- 425 Humphreys, E. D., Schmandt, B., Bezada, M. J., & Perry-Houts, J. (2015). Recent craton growth by slab  
426 stacking beneath Wyoming. *Earth Planet. Sci. Lett.*, *429*, 170–180, doi: 10.1016/j.epsl.2015.07.066.
- 427 Jackson, M. G., Konter, J. G., & Becker, T. W. (2017). Primordial helium entrained by the hottest mantle  
428 plumes. *Nature*, *542*, 340–343, doi: 10.1038/nature21023.
- 429 Keifer, I., & Dueker, K. (2019). Testing the hypothesis that temperature modulates 410 and 660 dis-  
430 continuity topography beneath the eastern United States. *Earth Planet. Sci. Lett.*, *524*, 115723, doi:  
431 10.1016/j.epsl.2019.115723.
- 432 Kennett, B. L. N., & Engdahl, E. R. (1991). Traveltimes for global earthquake location and phase identifi-  
433 cation. *Geophys. J. Int.*, *105*, 429–465, doi: 10.1111/j.1365-246X.1991.tb06724.x.
- 434 Kennett, B. L. N., Engdahl, E. R., & Buland, R. (1995). Constraints on seismic velocities in the Earth from  
435 traveltimes. *Geophys. J. Int.*, *122*, 108–124, doi: 10.1111/j.1365-246X.1995.tb03540.x.
- 436 King, S. D., & Anderson, D. L. (1998). Edge-driven convection. *Earth Planet. Sci. Lett.*, *160*, 289–296, doi:  
437 10.1016/S0012-821X(98)00089-2.
- 438 Kinney, S. T., MacLennan, S. A., Keller, C. B., Schoene, B., Setera, J. B., VanTongeren, J. A., & Olsen,  
439 P. E. (2021). Zircon U-Pb geochronology constrains continental expression of Great Meteor Hotspot

440 magmatism. *Geophys. Res. Lett.*, *48*, e2020GL091390, doi: 10.1029/2020GL091390.

441 Kojitani, H., Inoue, T., & Akaogi, M. (2016). Precise measurements of enthalpy of postspinel transition  
442 in Mg<sub>2</sub>SiO<sub>4</sub> and application to the phase boundary calculation. *J. Geophys. Res.*, *121*, 729–742, doi:  
443 10.1002/2015JB012211.

444 Laske, G., Masters, G., Ma, Z., & Pasyanos, M. (2013). Update on CRUST1.0 — A 1-degree global model  
445 of Earth’s crust. *Geophys. Res. Abstracts*, *15*, EGU2013–2658.

446 Lawrence, J. F., & Shearer, P. M. (2006). A global study of transition zone thickness using receiver functions.  
447 *J. Geophys. Res.*, *111*, B06307, doi: 10.1029/2005JB003973.

448 van der Lee, S., Regenauer-Lieb, K., & Yuen, D. A. (2008). The role of water in connecting past and future  
449 episodes of subduction. *Earth Planet. Sci. Lett.*, *273*, 15–27, doi: 10.1016/j.epsl.2008.04.041.

450 Lei, W., Ruan, Y., Bozdağ, E., Peter, D., Lefebvre, M., Komatitsch, D., Tromp, J., Hill, J., Podhorszki, N.,  
451 & Pugmire, D. (2020). Global adjoint tomography–model GLAD-M25. *Geophys. J. Int.*, *223*, 1–21, doi:  
452 10.1093/gji/ggaa253.

453 Levin, V., Long, M. D., Skryzalin, P., Li, Y., & López, I. (2018). Seismic evidence for a recently formed  
454 mantle upwelling beneath New England. *Geology*, *46*, 87–90, doi: 10.1130/G39641.1.

455 Levin, V., Menke, W., & Park, J. (2000). No regional anisotropic domains in the northeastern US Appalachi-  
456 ans. *J. Geophys. Res.*, *105*, 19029–19042, doi: 10.1029/2000JB900123.

457 Li, A., Fischer, K. M., Wysession, M. E., & Clarke, T. J. (1998). Mantle discontinuities and temperature  
458 under the North American continental keel. *Nature*, *395*, 160–163, doi: 10.1038/25972.

459 Ligorria, J. P., & Ammon, C. J. (1999). Iterative deconvolution and receiver-function estimation. *B. Seis-  
460 mol. Soc. Am.*, *89*, 1395–1400, doi: 10.1785/BSSA0890051395.

461 Long, M. D., Benoit, M. H., Chapman, M. C., & King, S. D. (2010). Upper mantle anisotropy and transition  
462 zone thickness beneath southeastern North America and implications for mantle dynamics. *Geochem. Geophys. Geosys.*, *11*, doi: 10.1029/2010GC003247.

463 Long, M. D., Jackson, K. G., & McNamara, J. F. (2016). SKS splitting beneath Transportable Array stations  
464 in eastern North America and the signature of past lithospheric deformation. *Geochem. Geophys. Geosys.*,  
465 *17*, 2–15, doi: 10.1002/2015GC006088.

466 Long, M. D., Levander, A., & Shearer, P. M. (2014). An introduction to the special issue of Earth and Plane-  
467 tary Science Letters on USArray science. *Earth Planet. Sci. Lett.*, *402*, 1–5, doi: 10.1016/j.epsl.2014.06.016.

468 Maguire, R., Ritsema, J., & Goes, S. (2018). Evidence of subduction-related thermal and compositional  
469 heterogeneity below the United States from transition zone receiver functions. *Geophys. Res. Lett.*, *45*,  
470 8913–8922, doi: 10.1029/2018GL078378.

471 Mao, W., Gurnis, M., & Wu, W. (2022). On the origin of small-scale seismic scatters at 660-km depth.  
472 *Geochem. Geophys. Geosys.*, *23*, e2022GC010560, doi: 10.1029/2022GC010560.

473 Mazza, S. E., Gazel, E., Bizimis, M., Moucha, R., Béguelin, P., Johnson, E. A., McAleer, R. J., & Sobolev,  
474 A. V. (2019). Sampling the volatile-rich transition zone beneath Bermuda. *Nature*, *569*, 398–403, doi:  
475 10.1038/s41586-019-1183-6.

476 Mazza, S. E., Gazel, E., Johnson, E. A., Kunk, M. J., McAleer, R., A, J. S., Bizimis, M., & Coleman,  
477 D. S. (2014). Volcanoes of the passive margin: The youngest magmatic event in eastern North America.  
478 *Geology*, *42*, 483–486, doi: 10.1130/G35407.1.

479 Menke, W., Skryzalin, P., Levin, V., Harper, T., Darbyshire, F., & Dong, T. (2016). The northern  
480 Appalachian anomaly: A modern asthenospheric upwelling. *Geophys. Res. Lett.*, *43*, 10–173, doi:  
481 10.1002/2016GL070918.

482 Morgan, W. J. (1971). Convection plumes in the lower mantle. *Nature*, *230*, 42–43, doi: 10.1038/230042a0.

483 Muir, J. M. R., Zhang, F., & Brodholt, J. P. (2021). The effect of water on the post-spinel transition and  
484 evidence for extreme water contents at the bottom of the transition zone. *Earth Planet. Sci. Lett.*, *565*,  
485 116909, doi: 10.1016/j.epsl.2021.116909.

486 Nelson, K. D. (1992). Are crustal thickness variations in old mountain belts like the Appalachi-  
487 ans a consequence of lithospheric delamination? *Geology*, *20*, 498–502, doi: 10.1130/0091-  
488 7613(1992)020<0498:ACTVIO>2.3.CO;2.

489 Page, M. T., & Hough, S. E. (2014). The New Madrid Seismic Zone: Not dead yet. *Science*, *343*, 762–764,  
490 doi: 10.1126/science.1248215.

491 Savage, B. (2021). Body wave speed structure of eastern North America. *Geochem. Geophys. Geosys.*, *22*,  
492 e2020GC009002, doi:10.1029/2020GC009002.

493

- 494 Schaeffer, A. J., & Lebedev, S. (2014). Imaging the North American continent using waveform inversion of  
495 global and USArray data. *Earth Planet. Sci. Lett.*, *402*, 26–41, doi: 10.1016/j.epsl.2014.05.014.
- 496 Schmandt, B., & Lin, F.-C. (2014). *P* and *S* wave tomography of the mantle beneath the United States.  
497 *Geophys. Res. Lett.*, *41*, 6342–6349, doi: 10.1002/2014GL061231.
- 498 Shearer, P. M., & Buehler, J. (2019). Imaging upper-mantle structure under USArray using long-period  
499 reflection seismology. *J. Geophys. Res.*, *124*, 9638–9652, doi: 10.1029/2019JB017326.
- 500 Sigloch, K. (2011). Mantle provinces under North America from multifrequency *P* wave tomography.  
501 *Geochem. Geophys. Geosys.*, *12*, doi: 10.1029/2010GC003421.
- 502 Sigloch, K., McQuarrie, N., & Nolet, G. (2008). Two-stage subduction history under North America inferred  
503 from multiple-frequency tomography. *Nature Geosci.*, *1*, 458–462, doi: 10.1038/ngeo231.
- 504 Simmons, N. A., Forte, A. M., Boschi, L., & Grand, S. P. (2010). GyPSuM: A joint tomographic model of  
505 mantle density and seismic wave speeds. *J. Geophys. Res.*, *115*, B12310, doi: 10.1029/2010JB007631.
- 506 Simmons, N. A., Myers, S. C., Johannesson, G., & Matzel, E. (2012). LLNL-G3Dv3: Global *P* wave  
507 tomography model for improved regional and teleseismic travel time prediction. *J. Geophys. Res.*, *117*,  
508 B10302, doi: 10.1029/2012JB009525.
- 509 Simmons, N. A., Myers, S. C., Morency, C., Chiang, A., & Knapp, D. R. (2021). SPiRaL: a multiresolution  
510 global tomography model of seismic wave speeds and radial anisotropy variations in the crust and mantle.  
511 *Geophys. J. Int.*, *227*, 1366–1391, doi: 10.1093/gji/ggab277.
- 512 Sleep, N. H. (1990). Hotspots and mantle plumes: Some phenomenology. *J. Geophys. Res.*, *95*, 6715–6736,  
513 doi: 10.1029/JB095iB05p06715.
- 514 van Stiphout, A. M., Cottaar, S., & Deuss, A. (2019). Receiver function mapping of mantle transition zone  
515 discontinuities beneath Alaska using scaled 3-D velocity corrections. *Geophys. J. Int.*, *219*, 1432–1446,  
516 doi: 10.1093/gji/ggz360.
- 517 Torgersen, T., Drenkard, S., Stute, M., Schlosser, P., & Shapiro, A. (1995). Mantle helium in ground  
518 waters of eastern North America: Time and space constraints on sources. *Geology*, *23*, 675–678, doi:  
519 10.1130/0091-7613(1995)023<0675:MHIGWO>2.3.CO;2.
- 520 Vogt, P., & Jung, W.-Y. (2007). Origin of the Bermuda volcanoes and the Bermuda Rise: history, observa-  
521 tions, models, and puzzles. *Geol. Soc. Am. Spec. Paper*, *430*, 553–591, doi: 10.1130/SPE430.
- 522 Wang, H., Zhao, D., Huang, Z., & Wang, L. (2019). Tomography, seismotectonics, and mantle dynamics of  
523 central and eastern United States. *J. Geophys. Res.*, *124*, 8890–8907, doi: 10.1029/2019JB017478.
- 524 Wu, W., Ni, S., & Irving, J. C. E. (2019). Inferring Earth’s discontinuous chemical layering from the  
525 660-kilometer boundary topography. *Science*, *363*, 736–740. doi:10.1126/science.aav0822.
- 526 Yu, Y. G., Wu, Z., & Wentzcovitch, R. M. (2008).  $\alpha$ - $\beta$ - $\gamma$  transformations in  $\text{Mg}_2\text{SiO}_4$  in Earth’s transition  
527 zone. *Earth Planet. Sci. Lett.*, *273*, 115–122, doi: 10.1016/j.epsl.2008.06.023.
- 528 Zhang, H., Schmandt, B., Zhou, W.-Y., Zhang, J. S., & Maguire, R. (2022). A single 520 km disconti-  
529 nuity beneath the contiguous United States with pyrolitic seismic properties. *Geophys. Res. Lett.*, *49*,  
530 e2022GL101300, doi: 10.1029/2022GL101300.
- 531 Zhang, Z., Irving, J. C. E., Simons, F. J., & Alkhalifah, T. (2023). Seismic evidence for a 1000 km mantle  
532 discontinuity under the Pacific. *Nat. Commun.*, (p. in revision).